RESEARCH ARTICLE

A microphysical investigation of different convective cells during the precipitation event with sustained high-resolution observations

Ziheng HUANG[1,2,3]**, Zheng RUAN** (✉)[1]**, Debin SU** (✉)[2]

1 State Key Laboratory of Severe Weather, Chinese Academy of Meteorological Sciences, Beijing 100081, China
2 College of Electronic Engineering, Chengdu University of Information Technology, Chengdu 610225, China
3 Key Laboratory of Atmospheric Sounding, China Meteorological Administration, Chengdu 610225, China

Abstract The growth and breakup processes of raindrops within a cloud influence the rain intensity and the sizes of raindrops on the surface. The Doppler velocity spectrum acquired by a vertically pointing radar (VPR) contains information on atmospheric turbulence and the size classification of falling hydrometeors. In this study, the four types of Convective Cells (CC) during precipitation events with more than 700 mm of precipitation in southern China are described. The characteristics of four types of CCs correspond to the isolated convection, the early stage, the mature stage, and the decline stage of organizational convection, in that order. Microphysical analysis using retrieval of vertical air motion (Vair) and raindrop evolution in clouds from Doppler velocity spectra collected by C-band VPR revealed the growth and breakup of falling raindrops with dynamic impact. Larger raindrops appear in the early stages and are accompanied by ice particles, which are impacted by the falling path's downdraft. Raindrop aggregation, which is primarily related to the alternation of updraft and downdraft, accounts for the mature stage's high efficiency of surface rainfall. The CCs in the decline stage originate from the shallow uplift in the weak and broad downdraft under conditions of enough water vapor. The updraft dominates the stage of isolated convection. Observations of convective cells could be more accurately represented in model evaluations.

Keywords cloud microphysics, convective systems, convective cell, vertically pointing radar observations, Doppler velocity spectrum

1 Introduction

Deep convection, transitional or mixed cloud types, and stratus contribute significantly to monsoon precipitation, but shallow convective clouds also play a significant role (Narayanan, 1967; Konwar et al., 2014; Saikranthi et al., 2014; Utsav et al., 2017). Because these clouds are affected by various microphysical processes, their vertical radar reflectivity profiles differ.

To better comprehend the microphysical processes of precipitating systems, accurate estimation of drop size distribution (DSD) is crucial. Detailed measurements of vertical precipitation structure are important for comprehending microphysical processes and lead to improved parameterization of numerical models for meteorological forecasting and cloud resolution, as well as more precise radar precipitation estimation (Zhang et al., 2006, 2008; Lim and Hong, 2010; Chen et al., 2011). For observers, understanding the relationship between radar measurements and DSD is a research area that deserves attention (Johnston et al., 2022). A significant problem for model developers is to depict, in some way, the enormously complex and poorly understood network of microscale processes occurring in actual clouds and precipitation that involve microphysics (Morrison et al., 2020). Work on understanding the DSD of CC in real clouds and precipitation, which includes microphysics, is ongoing.

A major difference in DSD is the microphysical processes caused by cloud structure. Many studies have shown that different clouds undergo different microphysical processes and therefore, their vertical profiles of radar reflectance and precipitation have different signatures (Rutledge and Houze, 1987; Parker and Johnson, 2000; Fu and Liu, 2001; Hirose and Nakamura, 2004; Liu and Zipser, 2013; Carr et al., 2017; Raut et al., 2021). When focusing on warm rain processes, the diversity of

polarization parameters also reflects the influence of precipitation microphysical processes on precipitation estimation (Carr et al., 2017). For example, when there are shallow strata clouds trapped under a stable layer at the lowest 2−5 km. Assuming updrafts < 4−6 m·s^{-1} (the fall speed of 1−2 mm diameter raindrops), all raindrops forming near the cloud top will fall quickly, accumulate, and grow as they descend. Radar reflectivity should increase downwards (Liu and Zipser, 2013).

Numerous investigations have demonstrated that vertical air motion (Vair) has a higher effect on raindrops in convective clouds, and that Vair plays a significant role in the modification of microphysical processes (Houze, 1989; Rauber and Tokay, 1991; Shupe et al., 2008; Hagos et al., 2010; Yano and Plant, 2015; Ahmed et al., 2016; Marion and Trapp, 2019; Ghate et al., 2021; Khain et al., 2022). In convective precipitation, heavy precipitation is typically associated with strong updrafts, whereas stratus precipitation in the anvil area is typically associated with weak updrafts (Houze, 1989; Hagos et al., 2010; Ahmed et al., 2016). Frequently, cold pools are associated with Vair. There is a substantial association between the updraft and downdraft width and the depth of cold pools (Marion and Trapp, 2019). In a more detailed study, Garrett correlates gamma distribution with Vair, which shows that stronger updrafts lead to higher concentrations of large raindrops and a peak in the size of distribution. Due to the fact that Vair has a substantial impact on the interaction of raindrops under different convections, determining their involvement in altering raindrops is essential for microphysical processes. In addition, the relationship between the raindrop spectrum and precipitation composition is necessary to accurately describe the microscopic physical processes in the model (Raut et al., 2021).

Considered to have a significant effect on climate development, energy transmission, and circulation systems, convective cells are characterized by a small horizontal scale and a short time scale. However, conventional detection data, because of low temporal resolution, and reanalysis data, due to meteorological parameters, are limited by the parameterization schemes and are difficult to carry out detailed research. Numerous aspects of cloud, weather, and climate modeling are susceptible to microphysical processes (e.g., Harris et al., 2001; Kober et al., 2015; Dziekan and Pawlowska, 2017; Surcel et al., 2017). Unquestionably, the study of microphysical processes in CCs will aid in the expansion of our understanding.

The VPR (Vertically Pointing Radar) is most compatible with observational data for the variability of microphysical processes. Radar data based on precipitation frequency bands are required for convective precipitation analysis. C-band (wavelength 5 cm) VPR equipped with frequency modulated continuous wave (C-FMCW) technology can detect several heights with high spatial-temporal resolution. This makes precipitation observation more typical than point observation or small-volume observation with disdrometers and micro-rain radars. The Doppler spectrum of C-FMCW, which is sensitive to both turbulence and precipitation signals in moderate and heavy precipitation, can better represent the microphysical changes of the CC process that do not need to be assumed by models.

Understanding the microphysical evolution of CCs, which are associated with the various convection systems and convection stages, is essential for accurate simulation/prediction in numerical models. Using sustained high-resolution VPR data, this work seeks to investigate the microphysical processes in a few typical convective cells. The complete precipitation event encompassing four types of CCs during the summer monsoon in southern China is described. Dynamic and raindrop evolution in the cloud using the retrieval results includes vertical air motion and DSD with Doppler velocity spectrum measured from precipitation VPR in this study. The four typical convective cell characteristics described in this article provide insights into the microphysical processes and pathways of precipitation.

In this article, we propose a reverse approach to first classify the samples observed by C-FMCW, obtain the aloft DSD instead of the microphysical parameters, and describe the microphysical processes taking place in the actual cloud. We give details about the observational equipment and algorithm (in Section 2), which captures aloft DSD and Vair from measured data, providing a more consistent description of surface DSD and microphysics. The characteristics of minute rainfall and the vertical convection structure are analyzed (in Section 3). Lastly, we analyze the microphysical processes for raindrop growth in the liquid water region and the influence of atmospheric motion (in Section 4) over the liquid water region using this methodology. Conclusions and discussions are presented in Section 5.

2   Instruments and method

The simultaneous observations of cloud and precipitation microphysics were made by C-FMCW and a disdrometer (OTT Parsivel), at the Cloud Precipitation Microphysics Super Observatory Station, Longmen County, Guangdong Province, (114°14′23.9″E, 23°46′48.0″N, 79 m). The site is one of the three highest frequency precipitation centers of Guangdong (He et al., 2016, Fig. 1). In addition, observation data consisting of a nearby weather radar network and a wind profiling radar at the same location are utilized.

2.1   Equipment

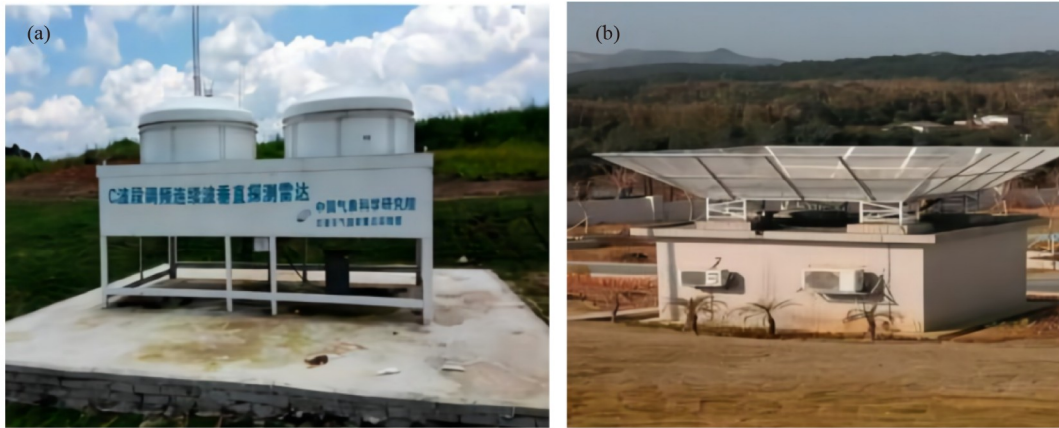One of the advantages of the C-FMCW in this study is

Fig. 1   (a) C-FMCW and (b) wind profiler.

that, unlike pulse radar, there is no blind height, and a single observation mode can observe the vertical continuous structure height from the surface to nearly cloud top. The initial level of VPR data is the Doppler velocity spectrum, which is transformed from time domain to frequency domain using fast fourier transform (FFT) by the signal processing algorithm. The Doppler velocity spectrum in the radar vertical beam contains the affection of Vair and the information of various size particles' fall speeds. For the vertically limited height, the reflectivity attenuation effect of C-FMCW observation is generally weak, particularly in the height below the melting level, which has a stronger relationship with surface rainfall characteristics. Compared with the weather scanning radar, the VPR can give the origin of surface DSD characteristics from microphysical processes happening in an aloft cloud. Table 1 provides further information on the C-FMCW.

2.2   Method

In the last decades, radar has been utilized to analyze Vair

and microphysical parameters. Researchers have devised numerous methodologies. The method developments followed two different paths, with significantly different philosophies. One involved using radar to directly describe microphysical processes, without sorting into theoretical models. The Doppler spectrum is a measure of the power per unit phase shift caused by motion (along the VPR beam) of the scatters in the detection volume, which is the result of the convolution of turbulence spectrum and raindrop spectrum. Assuming that the falling velocity is a function of the DSD, the DSD is closely related to the power spectrum (Babb et al., 1999). Thus, after separating the two spectra, the turbulence spectrum and the raindrop spectrum can be used to obtain Vair and the DSD. Profilers' ability to concurrently observe spectral peaks associated with clear-air Vair and peaks associated with hydrometeors enables the calculation of DSD (May and Keenan, 2005). The raindrop spectrum estimate approach, based on this principle, is widely used in VHF-band and UHF-band radars (Ecklund et al., 1999; Kirankumar et al., 2008; Yeung et al., 2021). Williams et al. (2016) and Pang et al. (2021) advanced Doppler spectrum-based DSD recognition.

The other category will rely more on the support of theoretical models, for example, methods based on the dual-frequency ratio (DFR). Based on higher frequencies, stronger non-Rayleigh backscattering can provide DSD characteristics. In particular, the DFR is independent of the concentration of raindrops and only depends on the size parameter and gamma parameterization of the DSD (Meneghini et al., 2022). Excluding the impacts of ice particles, melting layers, and hydrometeor attenuation, Munchak and Tokay (2008) calculated the DSD using DFR. Beauchamp et al. (2015) demonstrated that employing NASA's dual-frequency, dual-polarization Doppler radar data for high-resolution observations of heavy precipitation is effective. Finlon et al. (2022) correlated the variability in the cloud with microscopic physical processes, such as growth processes such as aggregation, and ultimately demonstrated an increase in DFR in multi-

Table 1   The operating parameters of C-FMCW

Index	Parameters	C-FMCW
1	Operating frequency	5530 MHz
2	Transmit type	Solid state
3	Transmitting power	>150 W
4	Antenna type	Parabolic
5	Antenna beamwidth	2.4°
6	Sampling interval	2−3 s
7	Interpulse period	700 μs
8	Range resolution	30 m
9	Detection range	0.03−15 km
10	No. of points in Spectrum	512
11	Spectral resolution	0.0895 m·s^{-1}
12	Detection mode	Fixed vertical pointing
13	Speed range	± 22.912 m·s^{-1}

frequency radar data. Despite the ambiguity in the DFR relationship can be handled analytically, it is not always possible to find an exact solution among the multitude of solutions, even when an accurate path-integrated loss estimate is available or when a consistency constraint is imposed (Meneghini et al., 2022). Considering the demanding time-space scale of CC for the algorithm, we employ the former method for reverse.

2.2.1 Doppler velocity spectrum of VPR

The Doppler velocity spectrum $S_{obs}(v,r)\left[\left(mm^6m^{-3}\right)\left(ms^{-1}\right)^{-1}\right]$ observed by the VPR at each range gate r is the convolution of raindrop spectrum $S_{DSD}(v-w,r)$, and turbulence spectrum $S_{air}(v,r)$. It can be given by the following formula:

$$S_{obs}(v,r) = S_{DSD}(v-w,r) \otimes S_{air}(v,r) + S_{noise}(v,r), \quad (1)$$

The $w\,(m\cdot s^{-1})$ refers to the mean V_{air}, $v\,(m\cdot s^{-1})$ refers to the Doppler velocity. $S_{noise}(v,r)$ represents the background noise and varies with the range gate r. We cannot directly obtain the distribution of raindrop spectrum and conduct quantitative analysis. In this article, the DC components and noise levels have been preprocessed. We use the segmentation method to estimate the noise level and use the interpolation method to remove the DC component in the Doppler velocity spectrum (Petitdidier et al., 1997).

In static air, the raindrop spectrum $S_{DSD}(v,r)$ can be expressed by the DSD and raindrop backscattering cross section $\sigma_b^\lambda(D)$ as

$$S_{DSD}(v,r) = \left[\frac{l^4}{\pi^5|K_w|^2}\sigma_b^\lambda(D)\right]N_{DSD}(D)\frac{dD}{dv}, \quad (2)$$

where λ is the wavelength of radar, $|K_w|^2$ is the dielectric factor and is set as a constant of 0.93. For a wavelength of 5.42 cm, Rayleigh scattering occurs at this time, and the raindrop can be regarded as spherical particles. $\sigma_b^\lambda(D)$ is proportional to the particle diameter by a power of 6 and can be expressed as

$$\sigma_b^\lambda(D) = \frac{\pi^5|K_w|^2}{\lambda^4}D^6. \quad (3)$$

Using the classical relationship between raindrop terminal velocity and diameter D (mm) derived from Atlas et al. (1973):

$$V(D) = \left[9.65 - 10.3\exp(-0.6D)\left(\frac{\rho_0}{\rho_h}\right)^{0.4}\right], \quad (4)$$

where ρ_h and ρ_0 denote the height h and the surface atmospheric density. $\frac{\rho_0}{\rho_h}$ is related to surface temperature, vertical lapse rate of atmospheric temperature, and height. Under low altitude conditions, it can be simplified into a function only related to height.

At the first moment of the pure raindrop spectrum, the falling rate of raindrops can be expressed as the following formula:

$$V_{DSD}(r) = \frac{\displaystyle\sum_{D_{max}}^{D_{min}} D^{\mu+6}\exp\left[-(\mu+4)\frac{D}{D_m}\right]v(D)\Delta D}{\displaystyle\sum_{D_{max}}^{D_{min}} D^{\mu+6}\exp\left[-(\mu+4)\frac{D}{D_m}\right]\Delta D}. \quad (5)$$

In the idealized case of Rayleigh backscattering, Sensitivity of these parameters to DSD is different, e.g., large raindrops dominate the reflectivity, but contribute little to the liquid water content (LWC). In contrast, cloud droplets contribute significantly to LWC (Vivekanandan et al., 2020). The formulas to calculate R, LWC, D_m, and N_w are not shown in this manuscript.

In this study, the retrieval algorithm in the cloud referred to the method suitable for the C-band VPR. The method logic is that the variability of Vair and DSD dominates the spectral difference between adjacent distance libraries. The effect of DSD changes can be confirmed by looking up the prepared table, and Vair is calculated by the cost function between distance libraries. Finally, spectral broadening correction is used with the observation of wind profiling radar (Pang et al., 2021).

2.2.2 Retrieval combined with surface DSD

Under the influence of updraft (downdraft), the retrieval raindrops will be underestimated (overestimated). e.g., A refined error analysis of the influence of Vair on DSD retrieval in the context of an uncorrected velocity of $1\,m\cdot s^{-1}$ indicates that the mistakes for rainfall rates can reach as high as 50 percent (Kirankumar et al., 2008).

The conditions that vertical air motion near the surface is zero in Pang's method. In this section, the method is improved by using ground DSD. The main supplement is the scattering spectrum of particles at the first aloft height in radar beam volume with the model established from ground DSD data.

The DSD can be expressed with the three-parameter gamma distribution:

$$N(D) = N_0 D^\mu \exp(-\Lambda D), \quad (6)$$

or expressed with the probability density of the raindrops as

$$N(D) = n_c\frac{\Lambda^{\mu+1}}{\Gamma(\mu+1)}e^{-\Lambda D}D^\mu, \quad (7)$$

where N_0, n_c, μ and Λ, are concentration of raindrops, intercept parameters, shape, and slope.

Another form of DSD is given by Willis (1984), called normalized gamma DSD, expressed as

$$N_{\text{DSD}}(D) = N_w \frac{6}{4^4} \frac{(\mu+4)^{\mu+4}}{\Gamma(\mu+4)} \left(\frac{D}{D_m}\right)^\mu \exp\left[-(4+\mu)\left(\frac{D}{D_m}\right)\right], \quad (8)$$

where N_w and D_m are normalized number concentration parameter and mass-weight mean diameter. Γ represents the Euler gamma function.

At the first gate, the raindrop spectrum $S_{\text{DSD}}(v,1)$ can be expressed by the surface DSD with Eq. (2) and Eq. (8) as

$$S_{\text{DSD}}(v,1) = \left[\frac{l^4}{\pi^5 |K_w|^2} \sigma_b^\lambda(D)\right] \times$$
$$N_w \frac{6}{4^4} \frac{(\mu+4)^{\mu+4}}{\Gamma(\mu+4)} \left(\frac{D}{D_m}\right)^\mu \exp\left[-(4+\mu)\left(\frac{D}{D_m}\right)\right] \frac{dD}{dv}, \quad (9)$$

where N_w, D_m, and μ can be calculated in real time with surface DSD.

The raindrop spectrum of range gate is normalized:

$$S_{\text{DSD}}^{\text{nor}}(v,r) = S_{\text{DSD}}(v,r)/\max[S_{\text{DSD}}(v,r)]. \quad (10)$$

After confirming the raindrop velocity difference, the location difference between $S_{\text{DSD}}^{\text{nor}}(v,r)$ and $S_{\text{DSD}}^{\text{nor}}(v,r+1)$ depends on the Vair. The Vair can be obtained by minimizing the Cost Function (CF) of $S_{\text{DSD}}^{\text{nor}}(v,r)$ and $S_{\text{DSD}}^{\text{nor}}(v,r+1)$.

$$\text{Cost function} = \sum_{v=v_{\min}}^{v_{\max}} \left[S_{\text{DSD}}^{\text{nor}}(v-w,r) - S_{\text{model}}^{\text{nor}}(v,r)\right]^2. \quad (11)$$

When CF is the minimum, the Vair is completely eliminated. The absolute value of Vair is the product of the number of moves and the speed resolution. If $S_{\text{DSD}}^{\text{nor}}(v,r+1)$ moves to the right to get the minimum CF, it indicates that the air motion is updraft, otherwise downdraft.

2.2.3 Retrieval scheme

Following are the diagrams of Vair and microphysical processes obtained from the power spectrum (Fig. 2).

The retrieval results for detected spectra at 8:22:40 LCT on June 6, 2020, are displayed. The Doppler velocity spectrum observed from the surface to 15 km and the raindrop velocity spectrum and raindrop spectrum obtained from 150 m to 4200 m are depicted in Figs. 3(a), 3(b), and 3(c), respectively (the speed downward is positive). As shown in Fig. 3(a), the ice particles are falling at approximately 1−2 m·s^{-1} and then accelerate to faster fall speeds as they melt into raindrop, the width of the spectrum through a narrow-widest-wider changed with height descent. Figure 3(b) depicts the reflectivity factor Doppler velocity spectra of the raindrop after Vair has been eliminated, as well as the mean Vair and particles' falling velocity depicted by black and red lines, respectively. The retrieval of raindrop distribution and height is shown in Fig. 3(c).

The retrieval algorithm in this study uses the continuous altitude of the radar spectrum to eliminate the effect of Vair. The estimated results of DSD are stable and reliable because of the observational data's precise spatial scale and high time resolution. The initial height is computed for the DSD model of retrieval by combining it with the surface DSD. Figure 4 shows the correlation of
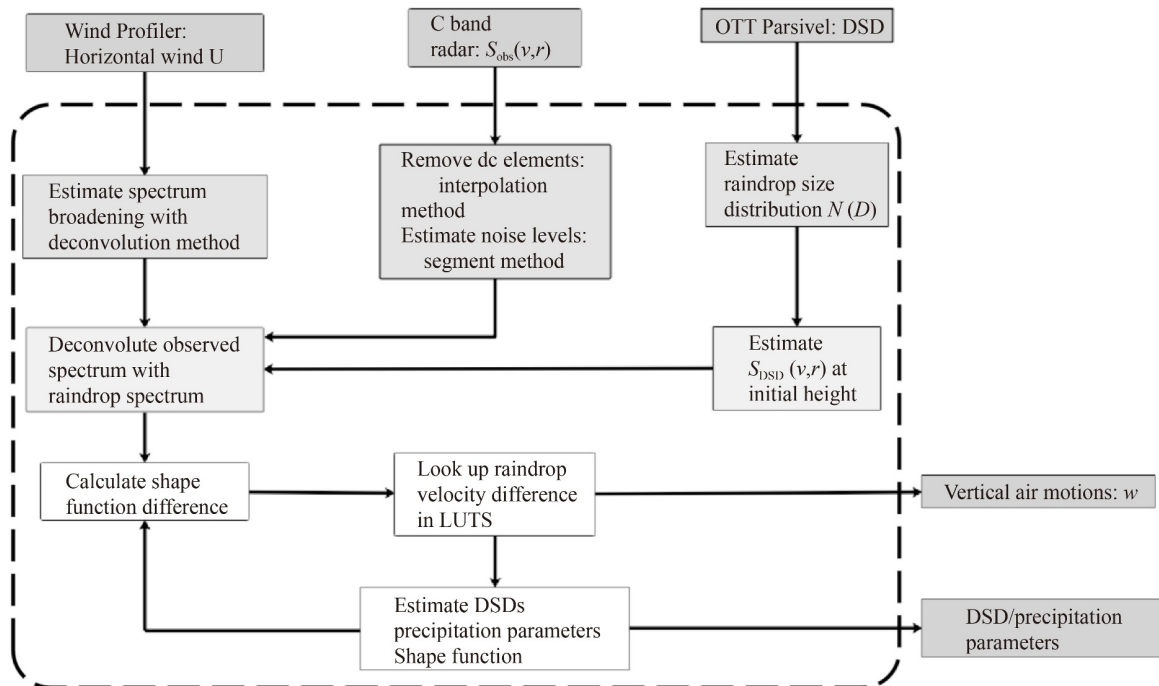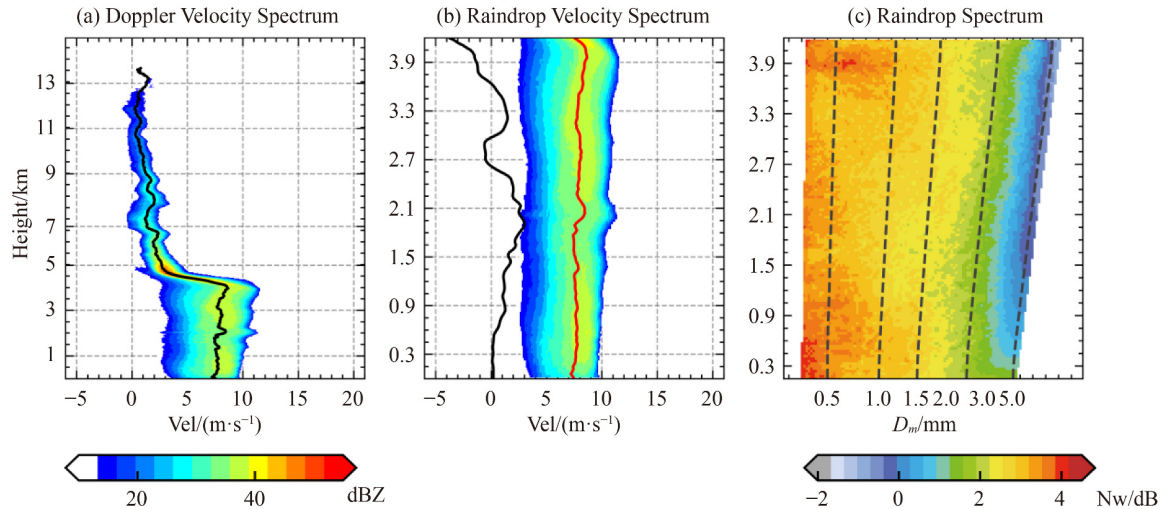

Fig. 2 Diagram of the retrieval algorithm.

Fig. 3 Profiles of reflectivity factor-weighted Doppler velocity spectral densities [10 log(mm^6·m^{-3}(m·s^{-1})$^{-1}$)] at 08:22:40 LCT on June 6, 2020. (a) Doppler velocity spectrum, (b) Raindrop Velocity Spectrum removed Vair (Vair with black line and mean fall speed with red line), and (c) Raindrop Spectrum.

the reflectivity factor and D_m between radar and OTT Parsivel, where the radar data height is 150 m. The correlations of reflectivity factor and D_m are 0.92 and 0.80, respectively, suggesting that cloud to ground uniformity exists.

3   Result and analysis

3.1   Convective cell in precipitation event

In 2020, the monsoon onset on May 20. With appropriate humidity, higher temperatures, and greater humidity, the extremely unstable atmosphere produces and sustains prolonged heavy rainfall. The total rainfall from June 6 to June 9 at the Longmen station in Guangdong Province, China, was 741 mm. 6847 samples collected with a disdrometer reveal the surface DSD characteristics and 151777 samples observed by C-FMCW reveal the

characteristics of microphysical processes within clouds.

In this long-term rainfall event, convective clouds and stratiform clouds contributed 71% and 29%, respectively, to the total precipitation and 51% and 49%, respectively, to the precipitation duration. This precipitation event was mostly fueled by intense but brief downpours. The synoptic systems were mesoscale convective systems (MCS), the predominant weather system during the monsoon season in southern China. The disparate properties of convective precipitation are reflected in the rainfall rate, particularly the disparity in rainfall intensity and duration represented by minute rain rate (MRR).

3.1.1   Identification of CC

To clearly demonstrate the precipitation characteristics and aloft microphysical processes of different convections in the precipitation process, four types of convective clouds specifically related to the CC are
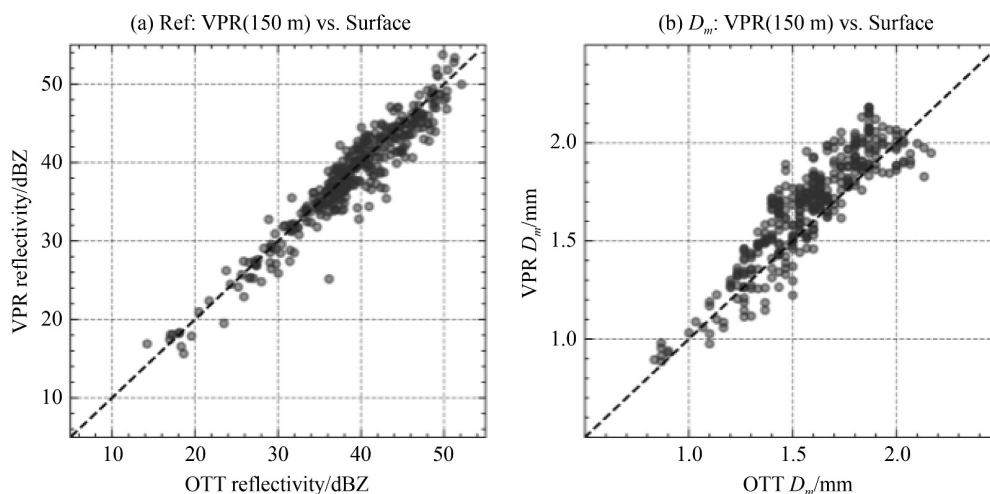

Fig. 4 Correlation of reflectivity factor (a) and D_m (b) calculated from C-FMCW and OTT Parsivel.

classified based on the vertical structure characteristics observed by C-FMCW and the surface MRR, concurrently combined with the composite reflectivity factor from the nearly operational weather radar network.

The number of defined types is susceptible to interpretation, however, the types are compatible with known climatic characteristics. According to the precipitation system given by the scanning radar, the four types of convection, which are isolated convective cell (ICC), deep convective cell (DCC), multi-convective cell (MCC), and mixed shallow cell (MSC).

In this paper, we selected the convective cell scale as the research object to reveal the microphysical characteristics of smaller-scale convection in the precipitation system. The four convections given in this study represent typical convective cell characteristics, where ICC represents isolated convective precipitation, and others are microphysical processes of precipitation that occurs in tissue convection. DCC represents the convective cell characteristics of the linear convective precipitation system, and MCC and MSC represent the convective cell characteristics in the mature stage and decay stage of the MCS precipitation system, respectively. At the same time, these four convective cells also represent four different convective precipitation microphysical processes. The ICC is an isolated convection triggered by the low-level updraft; DCC represents the microphysical process of precipitation in deep convection containing ice phase process. MCC represents the convection process in which the convection depth in the deep precipitation cloud extends to the height of the melting layer with mixed phase intervention. The MSC represents the shallow convection in deep precipitation clouds and the warm rain process. The purpose of this study is to give the differences in precipitation microphysical processes for these four different forms of convection. In the study, a precipitation process with a long precipitation time and large precipitation amount is used to present the above four convective precipitation microphysical processes.

The case of precipitation analyzed in the paper occurs in a more common precipitation center in southern China (He et al., 2016). The station's precipitation in the 2020 rainy season is 2090.6 mm, of which the contribution of convective precipitation is 68.4%. The convective precipitation contribution from ICC is 19.51%, MCC and MSC 26.71% and DCC 29.43%. The cumulative rainfall of this precipitation process is 741 mm, and four types of precipitation are the main precipitation manifestations of this precipitation process. Therefore, the analysis of even a precipitation process can represent the characteristics of micro-scale convective precipitation in the region, which is helpful to understand the convective cell-scale microphysical processes in several precipitation systems.

The composite radar reflectivity factor of weather radar network of 10:30 LCT on June 7. Houze (2018) describes

the canonical life cycle of a Mesoscale Convective System (MCS). Figure 5(a) depicts the distribution of four CCs in the precipitation system. A series of such convection cells appear in close vicinity is a key signature of the system in the early stage. This period of both active convection and stratiform precipitation marks the mature stage of MCS. After the mature stage, it is the decline stage of the system, and its basic feature is that the convection and the layered part of the MCS decrease together. Thus, we conclude that DCC is in the early stage of MCS, MCC is in the mature stage, and MSC is near to the decline stage of MCS. ICC is a shallow isolated convection triggered by residual perturbation after MCS removal. At the same time, these four convective cells also represent four different convective precipitation microphysical processes. The ICC is an isolated convection triggered by the low-level updraft. DCC represents the microphysical process of precipitation in deep convection containing ice phase process. MCC represents the convection process in which the convection depth in the deep precipitation cloud extends to the height of the melting layer with mixed phase intervention. The MSC represents the shallow convection in deep precipitation clouds and the warm cloud convection. The above characteristics of VPR are shown in Fig. 5(b).

The selected 60 min from June 7 to June 9 are displayed. Figure 6 displayed the characteristics of four types of small-scale convection. Figure 6 displays the reflectivity factor, measured vertical velocity, and Vair retrieval separately. Clearly, the features of cloud top, convective depth, and Vair are distinct.

As shown in Fig. 6(d), fluctuations in the MRR have a close relationship with Vair. The MRR can be sensitive to both reflectivity factor and Vair, and the peak of the MRR correlates frequently to the advent of a strong downdraft in the region of strong echo. Table 2 provides more information on four types.

3.1.2 Rainfall characteristics of CC

The characteristics of surface precipitation of four kinds of convection are described by the MRR and DSD. The four grades: slight, moderate, intense and extreme are divided according to the intensity of MRR (Zeng et al., 2021).

Figure 7(a) depicts the MRR intensity characteristics of four types of convection after normalization. It exhibited an unusually high average precipitation rate of over 0.5 mm·min^{-1} over MCC, which persisted for an extended duration. A significant increase in MRR to about 1.0 mm·min^{-1} throughout both ICC and DCC is indicative of the paroxysmal nature of precipitation. The MRR of MSC maintained a range of practically under 0.5 mm·min^{-1} and exhibited noticeable spikes (0.5 mm·min^{-1}), indicating that the precipitation was
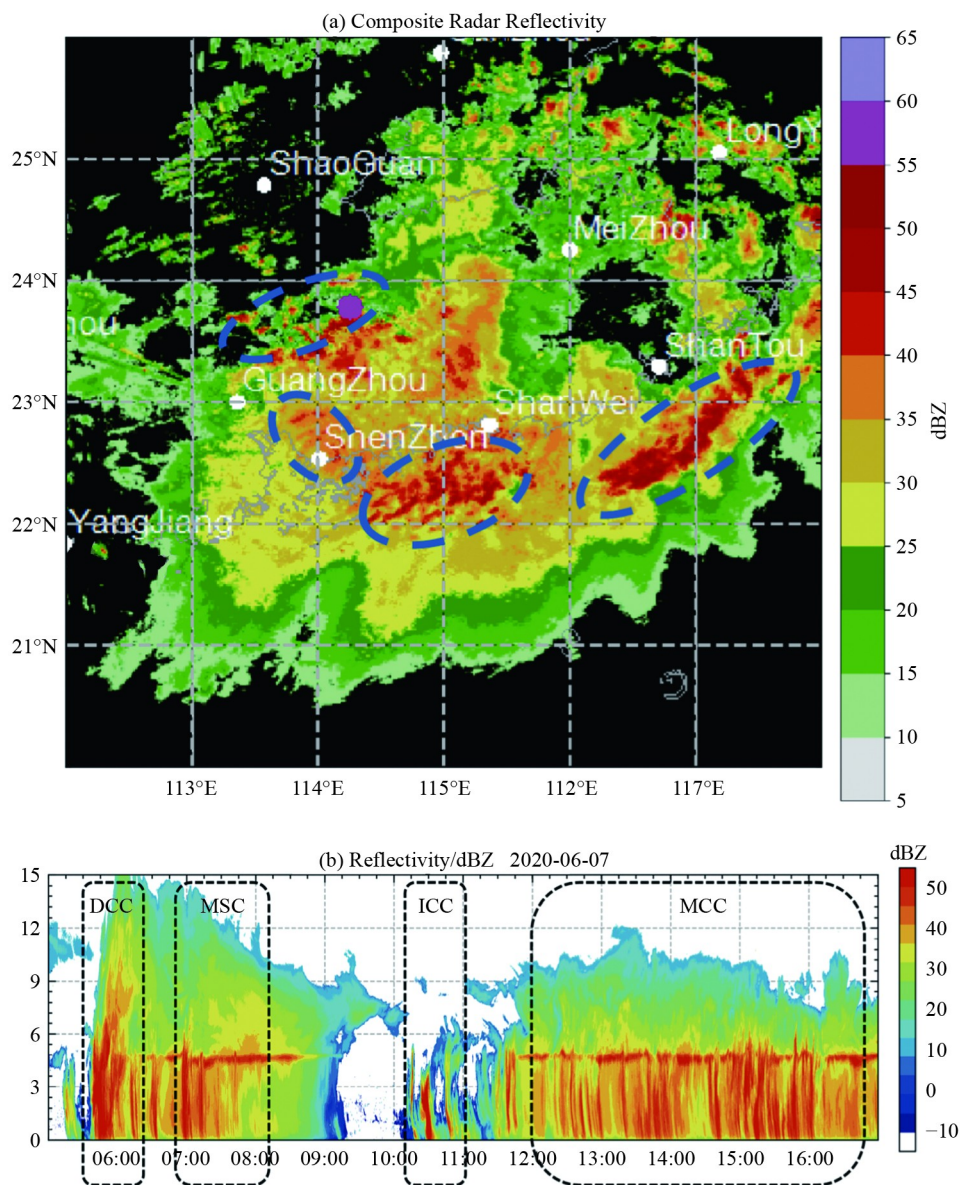
Fig. 5 (a) Composite radar reflectivity factor of South China Radar Network in Longmen Area (purple dot represents the station, white dots represent netted radars and marked areas represent different convections); (b) Time-height cross sections of reflectivity factor on June 7, 2020 LCT.

remarkable/particular. The MRR fraction was found to increase from moderate to extreme compared to impulsive rainfall, while it increased significantly in MCC (Fig. 7(b)).

Figure 7(c) showed the general correlation between the reflectivity factor and MRR. To some extent, it might be easier for MCC to induce a relatively high MRR (e.g., the intense to extreme). It should be clear that not all light MRRs were caused by weak convection and some of them were due to reflectivity factor (> 35 dBZ).

These distributions of D_m and $\lg N_w$ are important for the detailed interpretation of DSD results that usually represent regional precipitation properties (Fig. 7(d)). Note that under the influence of the summer monsoon, southern China has abundant low-level moisture, which is

usually different from the environmental conditions in other continental regions (Xu et al., 2009). The difference of DSD mentioned in this paper is more from the change of microphysical process caused by small-scale convection and Vair.

3.2 Vertical structure of CCs

The cloud top and convection depth are provided to aid comprehension of the differences in cloud and convective characteristics across the four types (Fig. 8(a)). Both DCC and MCC have substantially higher cloud tops, especially DCC. Under the impact of the precipitation system's updrafts, the cloud top altitude of DCC approached 15 km. The cloud top dispersion of MSC is
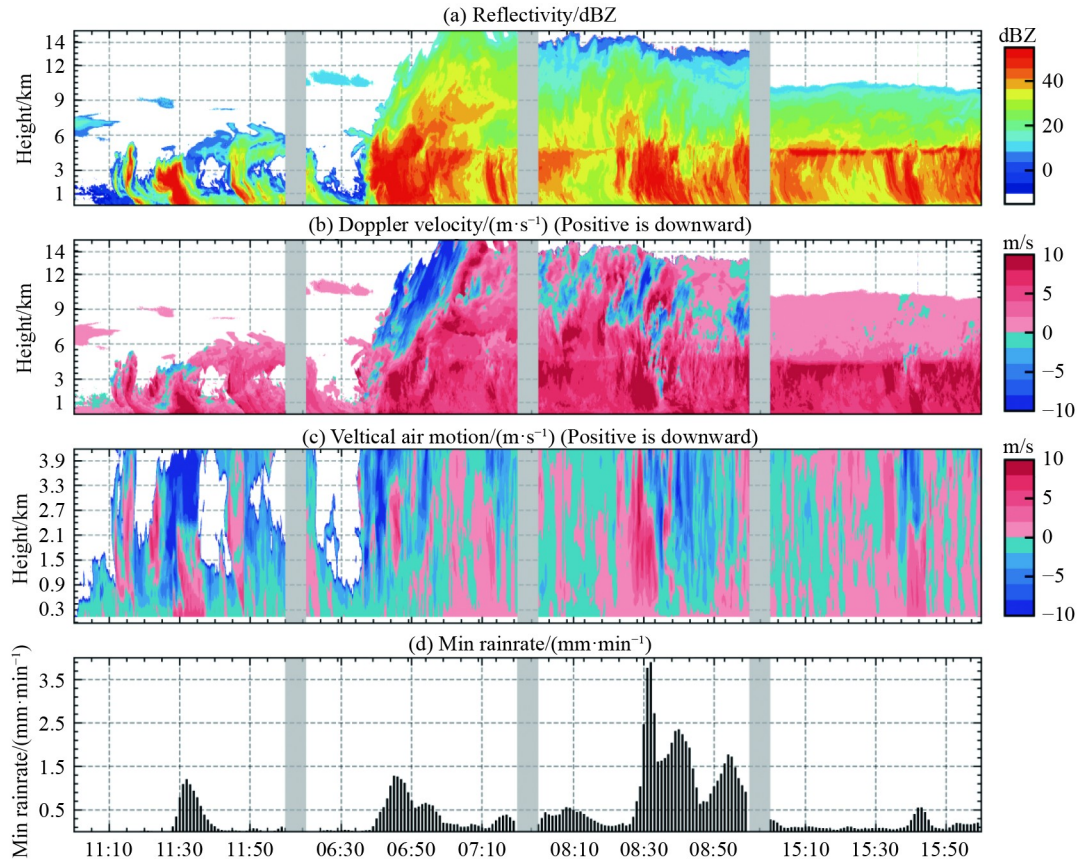
Fig. 6 Timing diagram of reflectivity factor, radial velocity, retrieved Vair, and MRR (top to bottom) for the four typical convective characteristics of ICC, DCC, MCC and MSC (left to right).

Table 2 Characterizes for four kinds

Kinds	Reflectivity factor	Radial velocity	Vair	MRR
ICC	Intense and fleeting	Positive main, mixed with negative	Updrafts dominant	Single stenosis peak
DCC	Intense and wider	First positive, then negative	First dominated by updrafts and then dominated by downdrafts	Single stenosis peak
MCC	Intense and widest	Alternation of positive and negative	Alternation of updraft and downdraft	Multiple peaks (maximum value)
MSC	weak with bright band	Positive main	Downdrafts dominant	Smooth with no obvious peak

clearly broader. The cloud top decreases as the development stage approaches the decline stage, which is consistent with Bouniol et al. (2016). As it continues to develop, as the cloud rolls in dry air from above the cloud top, Vair generates an updraft above the melting layer, causing the cloud top to rise (Hartmann, 2016). The convective top of the ICC is relatively close to the cloud top, indicating that convection has a strong influence on microphysical processes around the cloud top. In addition to the cloud top, the MCC and DCC convections are deeper, the microphysical processes are partly influenced by ice particles. The ICC and MSC are mostly shallow convection. The difference between the two is that the cloud top of the ICC is close to the convection depth, and MSC is the shallow convection under the deep cloud top and clear bright band.

Generally, the vertical structure can be divided into two

areas below the melting layer ($\sim$ 4.5 km) and above the melting layer. The size of the hydrometeor increases through deposition, maturation, and aggregation above the melting layer and through the mechanism of collision coalescence below the melting layer (Houze, 2014). In this study, we are more concerned with how changes below the melting layer (Fig. 8(b)). ΔZ(dBZ$_{3km}$– dBZ$_{0.5km}$) are given to understand the characteristics in microphysical processes between different precipitations. We chose the height range of 3−0.5 km to ensure that only liquid precipitation particles exist and discard the changes after the raindrops fall out of the clouds. ΔZ of DCC is notably biased toward the negative growth zone, which is consistent with the conclusion that deep convection may have a downward trend of radar reflectivity factor at near-earth height (Liu and Zipser, 2013). For the rest of the kinds, ΔZ is biased toward the
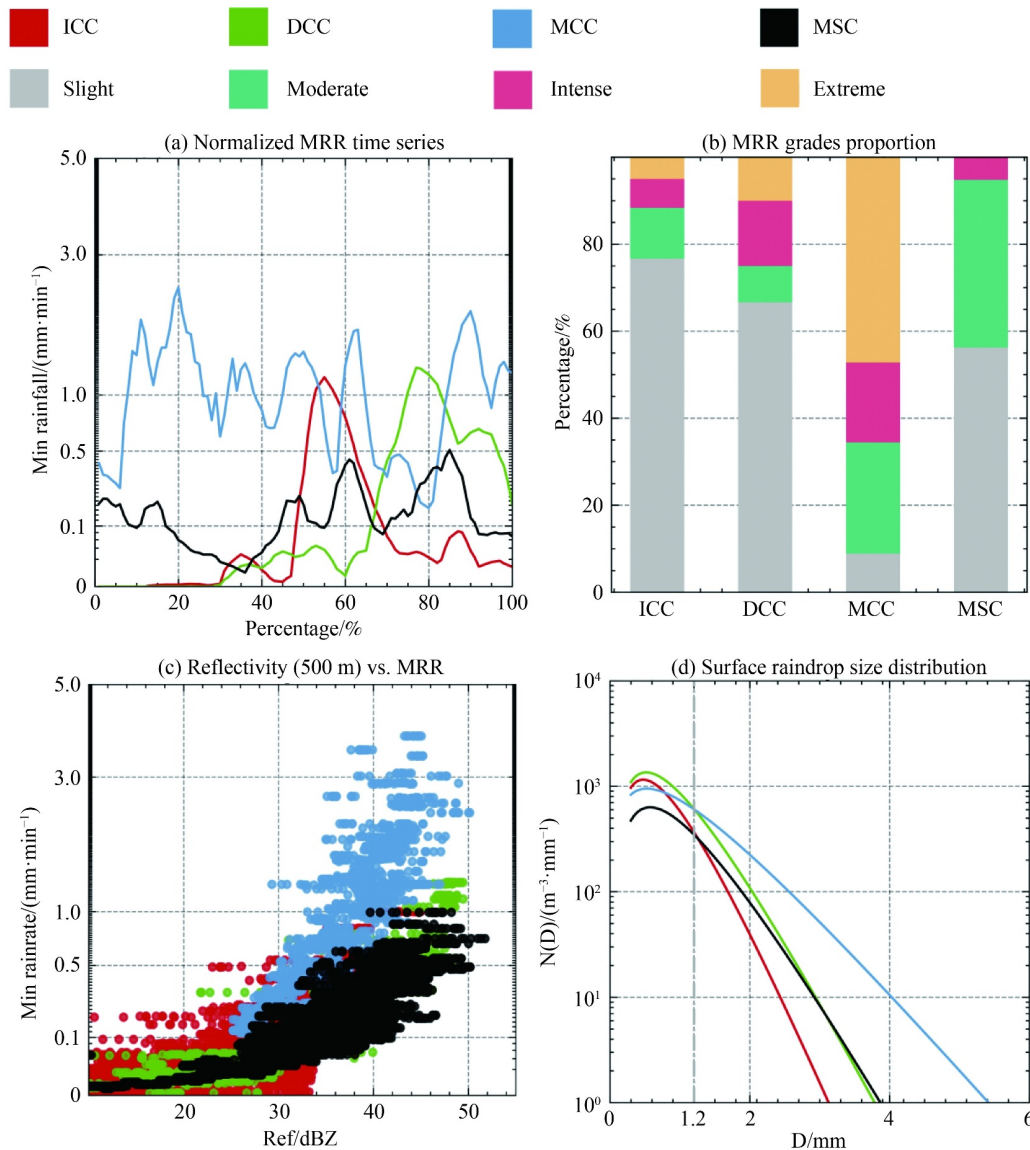
Fig. 7 (a) Normalized MRR timing diagram corresponding to different convection. (b) 100% stacked bar plots of different grades MRR corresponding to different convection. (c) Scatter diagram between radar reflectivity factor at 0.5 km above ground and MRR for different convections. (d) Centroids of the four-drop size distributions.

positive growth zone. In addition, the change of reflectivity factor for MSC is clearly more gradual.

3.3 Microphysical parameters in CCs

To understand the difference between various convections, the contoured frequency-by-altitude diagrams (CFADs) of the reflectivity factor are shown in Fig. 9(a). There are notably extensive and dispersive with CFAD of ICC, suggesting the strong and weak echoes coexist in the ICC, and the reflectivity factor changes greatly. For the rest of the convections, CFADs of Ref are sufficiently narrow and distinct, suggesting relatively stable cloud structure and microphysical Processes. Notable is the presence of the bright band in the MSC. The bright band created is a clear indication that MSC is transitioning

from the mature stage to the decline stage.

The distributions of D_m, N_w, and LWC (Figs. 9(b)−9(d)) are, in general, broader in ICC than other kinds, and a notably increasing trend of D_m (> 1.5 mm) and LWC on the falling path, suggesting a strong coalescence process. For the rest of the convections, the distributions of D_m, N_w, and LWC have roughly similar trends, the main difference is the position of the total value line. In general, the values of D_m, N_w, and LWC are larger in MCC, followed by DCC and MSC.

3.4 Microphysical vertical evolution processes

The differences in CFADs of D_m, $\lg N_w$, and $\lg$LWC (Figs. 9(b)−9(d)) are consistent with the differences in CFADs of Vair(Fig. 10(a)) (e.g., the Vair of MCC and
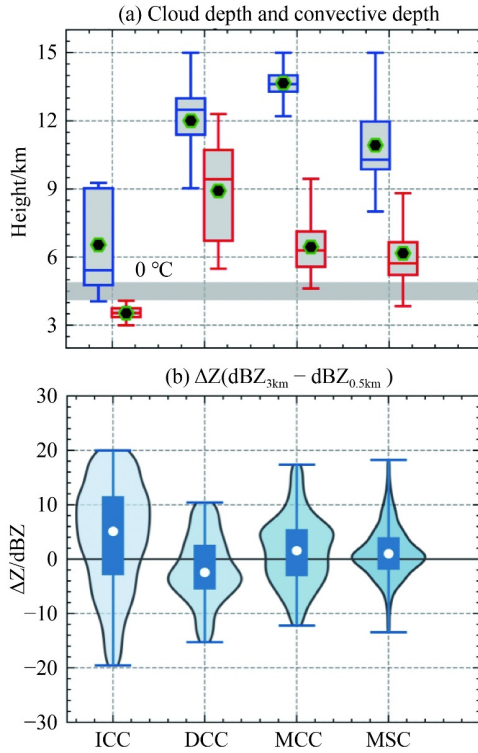
Fig. 8 Vertical structure characteristics of four kinds. (a) The cloud top height and convective top calculated from C-FMCW, with dot mark represents the mean value. (Cloud top: blue, Convective top: red). (b) Violinplot of ΔZ ($dBZ_{3km} - dBZ_{0.5km}$) corresponding to different convection.

MSC are similar, and D_m, lgN_w, and lgLWC are also similar), suggesting that the characteristics of microscopic physical processes are largely affected by Vair. These observations are qualitatively congruent with the spectrum of convective vertical velocity distributions established in earlier investigations (e.g., Wang et al., 2019, 2020). ICC is short-duration convection; hence, updrafts influence the beginning and maintenance of convection. Consistent with the conclusion of Bouniol et al. (2016), the Vair of ICC displays a clear updraft, however it is generally less than 4−6 m/s (the falling speed of raindrops with a diameter of 1−2 mm). DCC are characterized by updrafts (> 2 km) and downdrafts (2 km), which may be a result of the complicated airflow composition and wind shear in the front of the system (Zipser, 1977). Compared with the Vair of MCC and MSC, the existence of bright band structure makes the Vair of MSC more stable.

The reflectivity factor, D_m, N_w, and LWC depend on the DSD. The values of reflectivity factor, D_m, N_w, and LWC are more affected by bigger raindrops. To further comprehend the microphysical process, the DSD is provided. raindrops evaporate in the downdraft and form and grow in the updraft, which is a significant factor in the variation of reflectivity factor in warm rain areas. Combined with the Vair, we may explore qualitatively the

reasons for the changes in reflectivity factor caused by various microphysical processes.

In contrast, the relevant vertical profiles of raindrop concentration are shown in Fig. 10(b). The raindrops of the ICC, which form near the cloud's top, fall swiftly and grow as they descend. The increasing concentration of drops ($D\sim 1$ mm) below the melting layer demonstrates substantial coalescence processes on the fall path and the significant influence of warm rain processes from ICC in shaping surface DSD. Strong convective motion is sufficient to raise the freezing point of raindrops because in DCC, warm rain is suppressed (Albrecht, 1989; Rosenfeld et al., 2008), hence graupel melting is the primary source of rainwater reaching the surface. At a height of 3 km, this increases the number concentration of raindrops (1~ mm) to be significantly greater than other types. Due to the overall tilt of the cloud in DCC, the updraft at a higher height and the downdraft at a lower height dominate the Vair in DCC. The shift in reflectivity factor is brought on by the influence of Vair on DSD. The MCC in the precipitation system is consistent with the form proposed by Yang et al. (2015), which is a meso-β elongated convective system. Strong wind shear at lower levels increases the diameter of raindrops to 3.5 km. In MCC, the concentration of bigger raindrops ($D\sim 2.0$ mm) decreases below the melting layer. To the detriment of smaller raindrops ($D\sim 1$ mm), the concentration of large raindrops grows fast in the lower layers. The Vair of MSC is stable, for such weak convection, the updraft is less than the raindrop falling speed, which promotes the increase of the concentration of larger raindrops ($D\sim 2.0$ mm) below the melting layer, and the evaporation efficiency of smaller raindrops is greater than that of larger raindrops due to their greater surface area/mass ratio and slower falling speed. Since heavy raindrops dominate radar reflectivity factor, evaporation has a relatively minor effect on radar reflectivity factor.

To further compare and comprehend the microphysical processes in the air, Fig. 10(c) depicts the ground DSD. DSD near the surface (at 150 m) is essentially consistent with DSD at the surface. Note that, with the exception of the ICC, the other types of surface DSD have two high percentage cores, which is caused by the coexistence of updraft and downdraft in their Vair, and is most pronounced in the MCC surface DSD.

3.5 Surface DSD oriented analyses

In conclusion, the complex interaction of hydrometeors in clouds at various altitudes is critical for the formation of DSDs below the melt layer (Ryu et al., 2021). With the discussion of microphysical process, potential explanations for the observed difference in surface DSD are listed.

1) The ICC, shallow isolated convections, is triggered by residual disruption following the elimination of MCS.
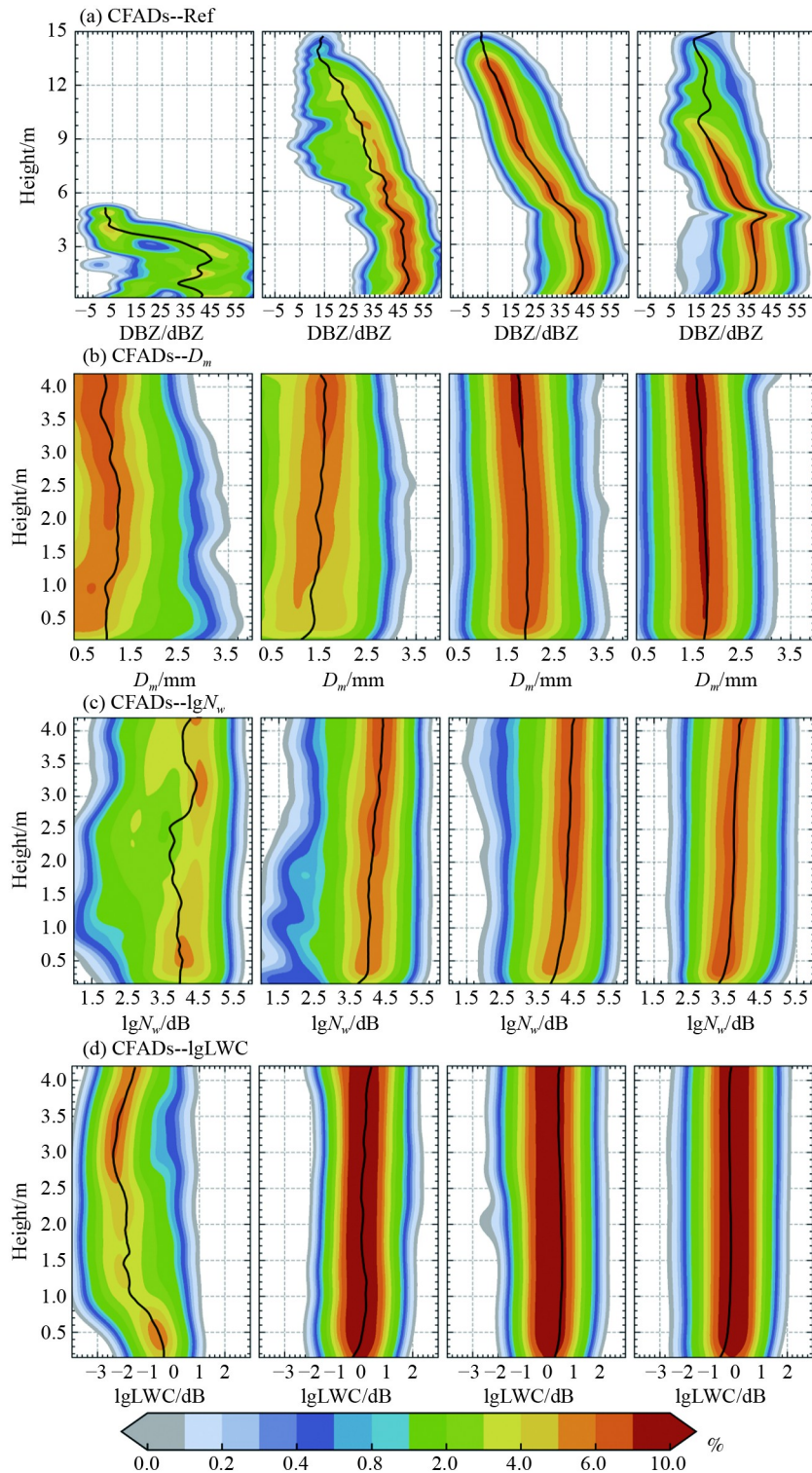
Fig. 9 The CFADs of reflectivity factor, D_m, $\lg N_w$, and lgLWC (top to bottom) for the different convection of ICC, DCC, MCC, and MSC (left to right). Black dashed lines show the mean of the distributions.

Raindrops formed near the top of the cloud fall quickly, dominated by the updraft and coalescence processes on the falling path. The radar reflectivity factor should increase downward. The concentration of smaller raindrops ($D < 1.2$ mm) is moderate, whereas the

concentration of larger raindrops ($D > 1.2$ mm) is low.

2) The DCC, deep convections in the early stage of MCS, cause graupel melting to be the primary source of precipitation reaching the surface. Along the falling path, raindrops transition from coalescence to breakup and
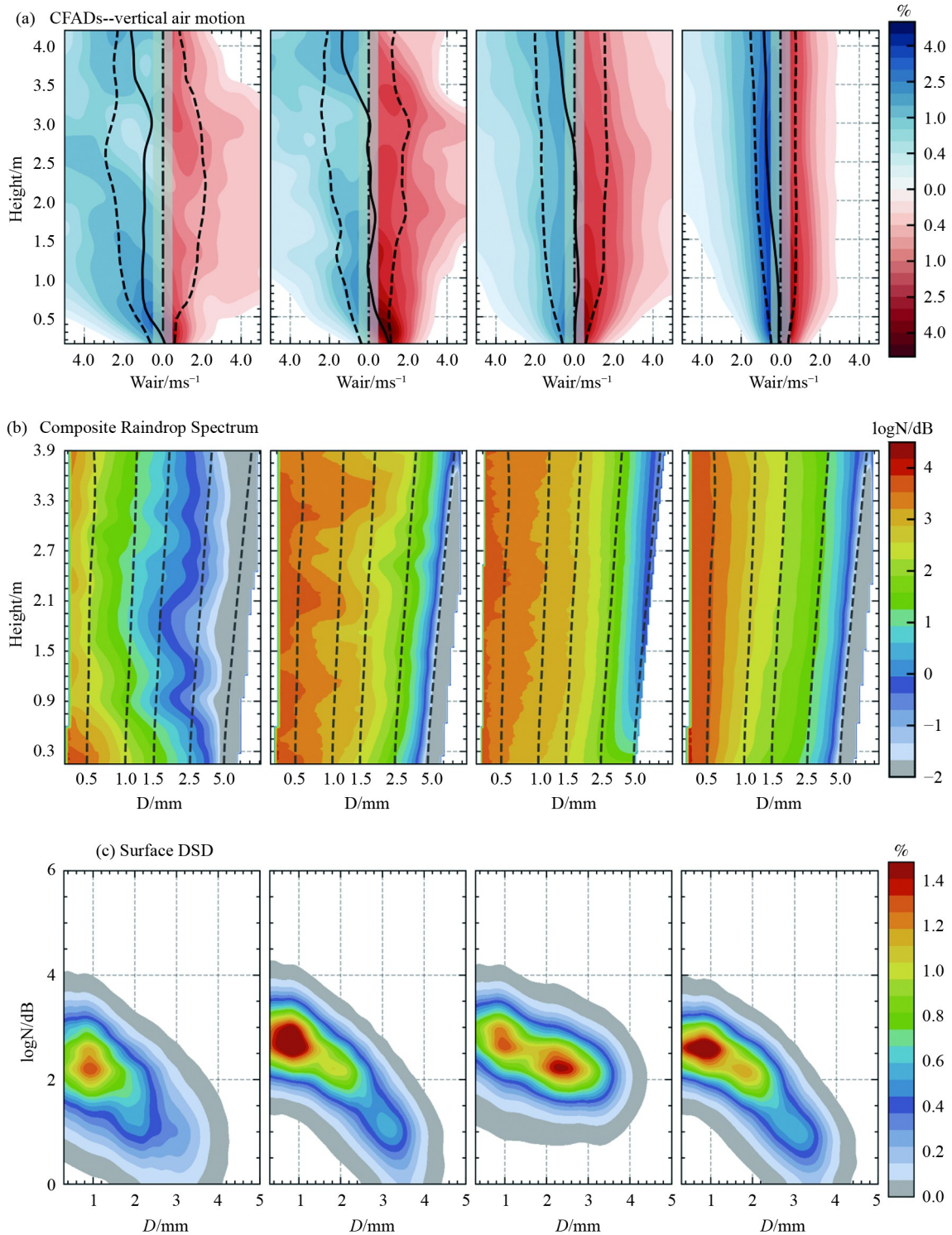
Fig. 10   (a) The CFADs of Vair, (b) composite DSD profiles, and (c) histogram of surface DSD for the different convection of ICC, DCC, MCC, and MSC (left to right).

evaporation, corresponding to changes in Vair. In particular, the low-level breakup and evaporation process somewhat surpassed the coalescence process, resulting in a downward trend in reflectivity factor. The concentration of smaller raindrops ($D < 1.2$ mm) is high, whereas the concentration of concentration of bigger raindrops ($D >$

1.2 mm) is moderate.

3) The MCC, multi-cell convections in the mature stage of MCS. DSD is comparable to DCC at 3 km altitude for the convection top above the bright band. The increase in reflectivity factor is caused by a general increase in the number concentration of bigger raindrops ($D\sim2.0$ mm)
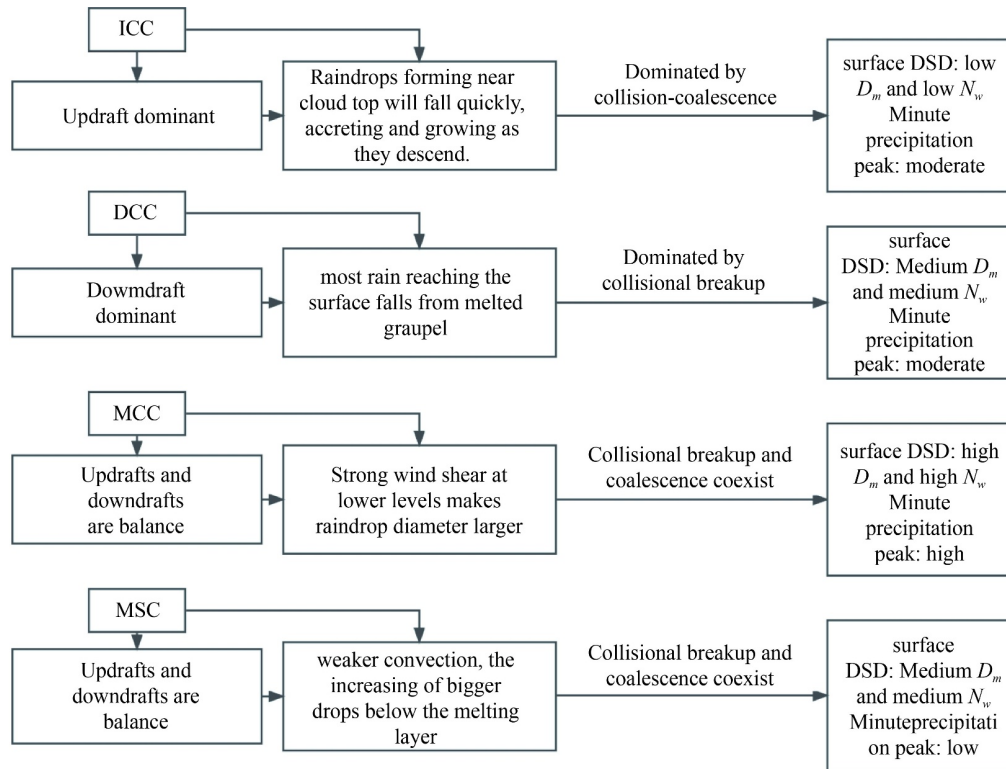
ICC → Updraft dominant → Raindrops forming near cloud top will fall quickly, accreting and growing as they descend. → Dominated by collision-coalescence → surface DSD: low D_m and low N_w Minute precipitation peak: moderate

DCC → Dowmdraft dominant → most rain reaching the surface falls from melted graupel → Dominated by collisional breakup → surface DSD: Medium D_m and medium N_w Minute precipitation peak: moderate

MCC → Updrafts and downdrafts are balance → Strong wind shear at lower levels makes raindrop diameter larger → Collisional breakup and coalescence coexist → surface DSD: high D_m and high N_w Minute precipitation peak: high

MSC → Updrafts and downdrafts are balance → weaker convection, the increasing of bigger drops below the melting layer → Collisional breakup and coalescence coexist → surface DSD: Medium D_m and medium N_w Minuteprecipitation peak: low

Fig. 11 The precipitation microphysics synthesis diagram of four convective kinds.

below the melting layer in MCC. The concentration of smaller raindrops ($D < 1.2$ mm) is moderate, whereas the concentration of bigger raindrops ($D > 1.2$ mm) is high.

4) The MSC, mixed stratiform convection, is close to the decline stage of MCS system. MSC's Vair is in a steady state. For weak convection, in which the updraft is less than the falling speed of raindrops, the concentration of larger raindrops (D 2.0 mm) below the melting layer increases, although the evaporation efficiency of smaller raindrops is greater than that of larger raindrops. Because the surface area/mass ratio is high and the falling velocity is low, the reflectivity factor range remains narrow. The concentration of smaller raindrops ($D < 1.2$ mm) is low, whereas the concentration of bigger raindrops ($D > 1.2$ mm) is moderate.

4 Discussion

The basic properties of multiple small-scale convections are necessary for understanding the vertical distribution of raindrops, convection life cycle, and precipitation efficiency. However, there are still major uncertainties in estimating the vertical distribution of raindrops and kinematic properties due to the limitation of observation methods and few studies on the kinematic and microphysical processes in convection based on observed data. Limited by an overly of complex and time-consuming retrieval methods, we can only give rigorous results for one case. In this manuscript, the retrieval results of microphysics and dynamic are in the same space-time in the cloud, and the reasonable retrieval scheme which decreases the influence of uncertainty output the interesting results for the convective clouds.

The four kinds of CCs characteristics in a precipitation event analyzed with C-FMCW, scanning radar, and ground raindrop distrometer. In combination with scanning radar, the microphysical processes within four types of CCs that correspond to different precipitation systems and convection phases may be clearly understood. High spatial and temporal resolution detection data of the Doppler velocity spectrum are used to retrieve the Vair and DSD in the liquid water region. We studied the relationship between surface DSD and the reflectivity of C-FMCW, Vair, and the vertical profile of DSD from kinematic and microphysical perspectives over a convective precipitation event. Major findings include as follow.

1) A more extensive analysis of convective characteristics can be more helpful for understanding complex precipitation systems. The height of the four kinds of convective cloud tops is more than 12 km except for isolated convection. DCC is located in the front of the precipitation system with the deepest convection depth, followed by the MCC convection depth in the mature stage. ICC and MSC are typically shallow convection. The isolated convective cloud top is near the convection depth, whereas the MSC is the shallow convection under the deep cloud top and the middle clear bright band. Overall, convection characteristics demonstrate a good

association with the convection life cycle. Regarding the relationship between MRR and convective intensity, most of the strong to extreme MRR is contributed by MCC, which is mostly related to the heavy raindrops of MCC. This agreed with the statistical results of Thomas et al. (2021) and their observation that the convective DSD mode diameter gradually shifts to a bigger raindrop size with increasing MRR. Also, not all of the light MRR was generated by the weak convection. This may result in part from coordination between large raindrops and small raindrops of unit mass, that is, a few larger raindrops creating significant radar reflectivity and smaller raindrops in moderation producing the slight MRR (Zeng et al., 2021).

2) For microphysical processes of different convections are influenced by both CC characteristics and Vair. ICC, shallow convection with a lower cloud top and updrafts < 4−6 m·s^{-1} (the fall speed of 1−2 mm diameter raindrops), any raindrops forming near cloud top will fall quickly. Microphysical processes show coalescence processes on the falling path. After the DCC is affected by the strong updraft, the downdraft dominates the main precipitation stage. Due to the inclined structure of the cloud, insufficient water vapor in front of a precipitation system, and the short convection period, the downdrafts do not contribute outstanding to the change of the MRR. MCC is clearly the strongest in terms of convective duration and cumulative precipitation, and its characteristics represent the convective characteristics of the mature stage of MCS in this area. The deep cloud top, the moderate depth convection with the convective top height of about 6 km and the active warm rain process are all related to the water vapor transport and strong dynamic disturbance caused by the alternation of updrafts and downdrafts. MSC, mixed stratiform convection, is nearing the decline stage of MCS. The Vair of MSC is stable. Influenced by the moist boundary layer in the monsoon, raindrops do not show considerable evaporation as expected in dry areas (Fabry and Zawadzki, 1995), hence the reflectivity is practically constant.

3) The precipitation intensity at different stages of the convective life cycle is visibly varied. One of the factors that cannot be ignored is the Vair. The Vair impacts the *Z-R* relationship by influencing the microphysical process, which has a major influence on the accuracy of radar precipitation estimation. The influence of air motions of precipitation has been concluded, In previous studies, the updraft will reduce the MRR, while downdraft will increase the MRR (Rajopadhyaya et al., 1998). In this study, the differences in physical quantities in updraft and downdraft are compared according to the differences in kinematical characteristics in four kinds of convection. In terms of this precipitation event, compared with the updraft, D_m changes slightly, N_w and Z are larger to a small extent, and the average MRR is significantly larger in the downdraft.

The comprehensive understanding of precipitation microphysics of the four kind CCs have been summarized in the synthesis diagram showed in Fig. 11.

Overall, this research, which is based on more meticulous observational data of a precipitation event with distinct CC characteristics, can improve our understanding of various CCs dynamics and microphysical processes, thereby improving the parameterization of microscale processes in climate models that occur in actual clouds and precipitation. At the same time, the understanding of the influence of atmospheric dynamics on the uncertainty in radar precipitation estimation has deepened.

References

Ahmed F, Schumacher C, Feng Z, Hagos S (2016). A retrieval of tropical latent heating using the 3D structure of precipitation features. J Appl Meteorol Climatol, 55(9): 1965–1982

Albrecht B A (1989). Aerosols, cloud microphysics, and fractional cloudiness. Science, 245(4923): 1227–1230

Atlas D, Srivastava R C, Sekhon R S (1973). Doppler radar characteristics of precipitation at vertical incidence. Rev Geophys, 11(1): 1–35

Babb D M, Verlinde J, Albrecht B A (1999). Retrieval of cloud microphysical parameters from 94-GHz radar Doppler power spectra. J Atmos Ocean Technol, 16(5): 489–503

Beauchamp R M, Chandrasekar V, Chen H, Vega M (2015). Overview of the D3R observations during the IFloodS Field experiment with emphasis on rainfall mapping and microphysics. J Hydrometeorol, 16(5): 2118–2132

Bouniol D, Roca R, Fiolleau T, Poan D E (2016). Macrophysical, microphysical, and radiative properties of tropical mesoscale convective systems over their life cycle. J Clim, 29(9): 3353–3371

Carr N, Kirstetter P E, Gourley J J, Hong Y (2017). Polarimetric signatures of midlatitude warm-rain precipitation events. J Appl Meteorol Climatol, 56(3): 697–711

Chen B, Hu W, Pu J (2011). Characteristics of the raindrop size distribution for freezing precipitation observed in southern China. J Geophys Res, 116(D6): D06201

Dziekan P, Pawlowska H (2017). Stochastic coalescence in Lagrangian cloud microphysics. Atmos Chem Phys, 17(22): 13509–13520

Ecklund W L, Williams C R, Johnston P E, Gage K S (1999). A 3-GHz profiler for precipitating cloud studies. J Atmos Ocean Technol, 16(3): 309–322

Fabry F, Zawadzki I (1995). Long-term radar observations of the melting layer of precipitation and their interpretation. J Atmos Sci, 52(7): 838–851

Finlon J A, McMurdie L A, Chase R J (2022). Investigation of microphysical properties within regions of enhanced dual-frequency

ratio during the IMPACTS field campaign. J Atmos Sci, 79(10): 2773–2795

Fu Y, Liu G (2001). The variability of tropical precipitation profiles and its impact on microwave brightness temperatures as inferred from TRMM data. J Appl Meteorol, 40(12): 2130–2143

Ghate V P, Cadeddu M P, Zheng X, O'Connor E (2021). Turbulence in the marine boundary layer and air motions below stratocumulus clouds at the ARM eastern North Atlantic site. J Appl Meteorol Climatol, 60(10): 1495–1510

Hagos S, Zhang C, Tao W, Lang S, Takayabu Y N, Shige S, Katsumata M, Olson B, L'Ecuyer T (2010). Estimates of tropical diabatic heating profiles: commonalities and uncertainties. J Clim, 23(3): 542–558

Harris D, Foufoula-Georgiou E, Droegemeier K K, Levit J J (2001). Multiscale statistical properties of a high-resolution precipitation forecast. J Hydrometeorol, 2(4): 406–418

Hartmann D L (2016). Tropical anvil clouds and climate sensitivity. Proc Natl Acad Sci, 113(32): 8897–8899

He L, Chen T, Kong Q (2016). A review of studies on prefrontal torrential rain in South China. J Appl Meteor Sci, 27(5): 559–569

Hirose M, Nakamura K (2004). Spatiotemporal variation of the vertical gradient of rainfall rate observed by the TRMM precipitation radar. J Clim, 17(17): 3378–3397

Houze R A (2014). Cloud Dynamics. New York: Academic Press

Houze R A Jr (1989). Observed structure of mesoscale convective systems and implications for large-scale heating. Q J R Meteorol Soc, 115(487): 425–461

Houze R A Jr (2018). 100 Years of Research on Mesoscale Convective Systems. Meteorological Monographs, 59: 17.1–17.54

Johnston P E, Williams C R, White A B (2022). Rain drop size distributions estimated from NOAA snow-level radar data. J Atmos Ocean Technol, 39(3): 353–366

Khain A, Pinsky M, Korolev A (2022). Combined effect of the Wegener–Bergeron–Findeisen mechanism and large eddies on microphysics of mixed-phase stratiform clouds. J Atmos Sci, 79(2): 383–407

Kirankumar N V P, Rao T N, Radhakrishna B, Rao D N (2008). Statistical characteristics of raindrop size distribution in southwest monsoon season. J Appl Meteorol Climatol, 47(2): 576–590

Kober K, Foerster A M, Craig G C (2015). Examination of a stochastic and deterministic convection parameterization in the COSMO model. Mon Weather Rev, 143(10): 4088–4103

Konwar M, Das S, Deshpande S, Chakravarty K, Goswami B (2014). Microphysics of clouds and rain over the Western Ghat. J Geophys Res Atmos, 119(10): 6140–6159

Lim K S S, Hong S Y (2010). Development of an effective double-moment cloud microphysics scheme with prognostic cloud condensation nuclei (CCN) for weather and climate models. Mon Weather Rev, 138(5): 1587–1612

Liu C, Zipser E J (2013). Why does radar reflectivity tend to increase downward toward the ocean surface, but decrease downward toward the land surface? J Geophys Res Atmos, 118(1): 135–148

Marion G R, Trapp R J (2019). The dynamical coupling of convective updrafts, downdrafts, and cold pools in simulated supercell thunderstorms. J Geophys Res Atmo, 124(2): 664–683

May P T, Keenan T D (2005). Evaluation of microphysical retrievals from polarimetric radar with wind profiler data. J Appl Meteorol, 44(6): 827–838

Meneghini R, Liao L, Iguchi T (2022). A generalized dual-frequency ratio (DFR) approach for rain retrievals. J Atmos Ocean Technol, 39(9): 1309–1329

Morrison H, van Lier-Walqui M, Fridlind A M, Grabowski W W, Harrington J Y, Hoose C, Korolev A, Kumjian M R, Milbrandt J A, Pawlowska H, Posselt D J, Prat O P, Reimel K J, Shima S, Diedenhoven B V, Xue L (2020). Confronting the challenge of modeling cloud and precipitation microphysics. J Adv Model Earth Systems, 12: e2019MS001689

Munchak S J, Tokay A (2008). Retrieval of raindrop size distribution from simulated dual-frequency radar measurements. J Appl Meteorol Climatol, 47(1): 223–239

Narayanan V (1967). Radar observation of a monsoon rain squall at Bombay. Mausam (New Delhi), 18(3): 397–402

Pang S, Ruan Z, Yang L, Liu X, Huo Z, Li F, Ge R (2021). Estimating raindrop size distributions and vertical air motions with spectral difference using vertically pointing radar. J Atmos Ocean Technol, 38(10): 1697–1713

Parker M D, Johnson R H (2000). Organizational modes of midlatitude mesoscale convective systems. Mon Weather Rev, 128(10): 3413–3436

Petitdidier M, Sy A, Garrouste J, Delcourt J (1997). Statistical characteristics of the noise power spectral density in UHF and VHF wind profilers. Radio Sci, 32(3): 1229–1247

Rajopadhyaya D K, May P T, Cifelli R C, Avery S K, Willams C R, Ecklund W L, Gage K S (1998). The effect of vertical air motions on rain rates and median volume diameter determined from combined UHF and VHF wind profiler measurements and comparisons with rain gauge measurements. J Atmos Ocean Technol, 15(6): 1306–1319

Rauber R M, Tokay A (1991). An explanation for the existence of supercooled water at the top of cold clouds. J Atmos Sci, 48(8): 1005–1023

Raut B A, Konwar M, Murugavel P, Kadge D, Gurnule D, Sayyed I, Todekar K, Malap N, Bankar S, Prabhakaran T (2021). Microphysical origin of raindrop size distributions during the Indian monsoon. Geophys Res Lett, 48: e2021GL093581

Rosenfeld D, Lohmann U, Raga G B, O'Dowd C D, Kulmala M, Fuzzi S, Reissell A, Andreae M O (2008). Flood or drought: how do aerosols affect precipitation? Science, 321(5894): 1309–1313

Rutledge S A, Houze R A Jr (1987). A diagnostic modelling study of the trailing stratiform region of a Midlatitude Squall Line. J Atmos Sci, 44(18): 2640–2656

Ryu J, Song H J, Sohn B J, Liu C (2021). Global distribution of three types of drop size distribution representing heavy rainfall from GPM/DPR measurements. Geophy Res Lett, 48: e2020GL090871

Saikranthi K, Narayana Rao T, Radhakrishna B, Rao S (2014). Morphology of the vertical structure of precipitation over India and adjoining oceans based on long-term measurements of TRMM PR. J Geophys Res Atmos, 119(13): 8433–8449

Shupe M D, Kollias P, Persson P O G, McFarquhar G M (2008). Vertical motions in arctic mixed-phase stratiform clouds. J Atmos

Sci, 65(4): 1304–1322

Surcel M, Zawadzki I, Yau M K, Xue M, Kong F (2017). More on the scale dependence of the predictability of precipitation patterns: extension to the 2009–13 CAPS spring experiment ensemble forecasts. Mon Weather Rev, 145(9): 3625–3646

Thomas A, Kanawade V P, Chakravarty K, Srivastava A K (2021). Characterization of raindrop size distributions and its response to cloud microphysical properties. Atmos Res, 249: 105292

Utsav B, Deshpande S M, Das S K, Pandithurai G (2017). Statistical characteristics of convective clouds over the Western Ghats derived from weather radar observations. J Geophys Res Atmos, 122(18): 10050–10076

Vivekanandan J, Ghate V P, Jensen J B, Ellis S M, Schwartz M C (2020). A technique for estimating liquid droplet diameter and liquid water content in stratocumulus clouds using radar and lidar measurements. J Atmos Ocean Technol, 37(11): 2145–2161

Wang D, Giangrande S E, Feng Z, Hardin J C, Prein A F (2020). Updraft and downdraft core size and intensity as revealed by radar wind profilers: MCS observations and idealized model comparisons. J Geophys Res: Atmosph, 125: e2019JD031774

Wang D, Giangrande S E, Schiro K, Jensen M P, Houze R A Jr (2019). The characteristics of tropical and midlatitude mesoscale convective systems as revealed by radar wind profilers. J Geophys Res Atmos, 124(8): 4601–4619

Williams C R, Beauchamp R M, Chandrasekar V (2016). Vertical air motions and raindrop size distributions estimated using mean Doppler velocity difference from 3- and 35-GHz vertically pointing radars. IEEE Trans Geosci Remote Sens, 54(10): 6048–6060

Willis P T (1984). Functional fits to some observed drop size distributions and parameterization of rain. J Atmos Sci, 41(9): 1648–1661

Xu Z, Fu C, Qian Y (2009). Relative roles of land–sea distribution and orography in Asian monsoon intensity. J Atmos Sci, 66(9): 2714–2729

Yang X, Fei J, Huang X, Cheng X, Carvalho L M V, He H (2015). Characteristics of mesoscale convective systems over China and its vicinity using geostationary satellite FY2. J Clim, 28(12): 4890–4907

Yano J I, Plant R S (2015). Chapter 11: Closure. In: Plant R Sand Yano J I, Eds. Parameterization of Atmospheric Convection, Vol. 1. World Scientific, 325–401

Yeung N K H, Sherwood S C, Protat A, Lane T P, Williams C (2021). A doppler radar study of convective draft lengths over Darwin, Australia. Mon Weather Rev, 149(9): 2965–2974

Zeng Z, Wang D, Chen Y (2021). An investigation of convective features and *Z-R* relationships for a local extreme precipitation event. Atmos Res, 250: 105372

Zhang G, Sun J, Brandes E A (2006). Improving parameterization of rain microphysics with disdrometer and radar observations. J Atmos Sci, 63(4): 1273–1290

Zhang G, Xue M, Cao Q, Dawson D (2008). Diagnosing the intercept parameter for exponential raindrop size distribution based on video disdrometer observations: model development. J Appl Meteorol Climatol, 47(11): 2983–2992

Zipser E J (1977). Mesoscale and convective–scale downdrafts as distinct components of squall-line structure. Mon Weather Rev, 105(12): 1568–1589